Supplementary Information for

Eutectic Electrolyte towards Ultralong-Lived Zn//V₂O₅ Cell: In-Situ Generated Gradient Solid–electrolyte Interphase

Chao Meng,[a] Wei-Dong He,[a] Hao Tan,[a] Xing-Long Wu,*[be] Hong Liu*[ad] and Jian-Jun Wang*[ac]

[a] State Key Lab of Crystal Materials, Shandong University, Jinan 250100, P. R. China

[b] MOE Key Laboratory for UV Light-Emitting Materials and Technology, and Faculty of Chemistry,

Northeast Normal University, Changchun 130024, P. R. China

[c] Shenzhen Research Institute, Shandong University, Shenzhen 518057, P. R. China

[d] Institute for Advanced Interdisciplinary Research (IAIR), University of Jinan, Jinan 250022, P. R. China

[e] Key Laboratory of Organo-Pharmaceutical Chemistry of Jiangxi Province, Gannan Normal University,

   Gan Zhou 341000, P. R. China

*E-mail: xinglong@nenu.edu.cn ; hongliu@sdu.edu.cn ; wangjianjun@sdu.edu.cn

1. Experimental and Computational Section

Materials. Divanadium pentoxide (V_2O_5) was purchased from Macklin. Zinc sulfate ($ZnSO_4 \cdot 7H_2O$) was purchased from Sinopharm Chemical Reagent Co., Lte. Hydrated Zinc tetrafluoroborate ($Zn(BF_4)_2 \cdot xH_2O$, chemically pure) and 1,2-Dimethoxyethane (DME, $\geq 98\%$) were purchased from Aladdin. Zn foil (20 μm and 200 μm, 99.99%) and Cu foil (20 un, 99.99%) were purchased from Shenzhen Kejing Star Technology.

Electrolyte preparation. 2 mol of $ZnSO_4 \cdot 7H_2O$ were dissolved in deionized water to obtain 1L of 2M $ZnSO_4$ electrolyte. The $Zn(BF_4)_2$/DME electrolyte was prepared by adding hydrated $Zn(BF_4)_2 \cdot 6H_2O$ into DME to obtain a 1 L solution with x mol (x=1, 2, 3 and 4), named xm ZBFD. The $Zn(BF_4)_2$ electrolyte was similarly prepared, but deionized water was used as the solvent instead of DME.

Preparation of electrodes and assembly of full cells. The cathode electrodes were fabricated by mixing the active materials (V_2O_5) with super P and polyvinylidene fluoride (PVDF) in a weight ratio of 8:1:1. The above mixture was then combined with an appropriate amount of N-methyl-2-pyrrolidone (NMP) to form a slurry under vigorous strring for 8 hours. The resulting slurry was then spread onto a Ti foil and carbon cloth (for high mass loading), dried in a vacuum oven at 80 °C overnight, leading to a mass loading of about 2 mg cm^{-2} and 5.7 mg cm^{-2}. Full cells were assembled in CR2032-type coin-cell, using zinc foil as an anode and glass fiber filter (Whatman, grade GF/A) as the separator.

Electrochemical testing

Battery performance was evaluated using CR2032 coin-type cells on a Neware BTS-4000 battery test system. Zn plating/stripping tests were conducted on Zn symmetrical cells in $ZnSO_4$ and ZBFD electrolytes, while Coulombic efficiency (CE) measurements were carried out on asymmetrical Zn//Cu cells. The corrosion behavior of Zn foil electrode was studied using an electrochemical workstation (CHI 760e) with a three-electrode system (Zn foil as the working electrode, Pt as the counter electrode, and Ag/AgCl as the

reference electrode). Tafel plots were measured by scanning between -0.3 and -1.6 V at 5 mV s^{-1}, and the hydrogen evolution performance was collected through linear sweep voltammetry (LSV) with a potential range of -1.0 ~ -2.2 V *vs.* Ag/AgCl at a scan rate of 5 mV s^{-1}. Electrochemical impedance spectroscopy (EIS) was implemented within a frequency range of 10^5 to 10^{-2} Hz. Full cells were cycled between 0.3 and 1.6 V vs. Zn/Zn^{2+}, and the specific capacities were determined based on the mass of active materials.

Materials characterization

The Zn metal electrodes were extracted from the cells, washed with deionized water and ethanol, and dried in a vacuum drying oven. Focused-ion-beam assistd scanning electron microscopy (FIB-SEM, Auriga) and transmission electron microscopy (TEM, Tecnai F20) were used to prepare cross-sections of the SEI layer and observe morphology and composition. The TEM test sample was obtained by FIB thinning to below 100 nm. Crystallographic data of samples were recorded by X-ray diffraction (XRD) on Bruker-D2 Advance, with Cu Kα radiation (λ = 1.5418 Å) at a scan rate of 0.02 °/s. Texture measurements were collected on a Bruker D8 advance X-ray diffractometer with Cu-K$_\alpha$ radiation (λ = 0.15418 nm). Two-dimensional grazing incidence X-ray diffraction (2D-GIXRD) was performed on a Rigaku-SmartLab X-ray diffractometer with a Cu Kα X-ray source and a 2D silicon array detector. The instrument operates with a parallel beam at a fixed Angle of 0.5° and 2D-GIXRD patterns were collected from 30-60° 2θ, with a step size of 0.02° and a scan speed of 5°/min. Optical surface profilometry images were measured by an optical profilometer (Veeco, NT9300). Raman spectroscopy was obtained using Renishaw-inVia-Reflex with a 532 nm diode-pumped solid-state laser between 4000 cm^{-1} and 200 cm^{-1}. ^{19}F NMR spectra were acquired on a Bruker Advance III 400 M NMR spectrometer. Differential Scanning Calorimeter (DSC) was conducted using liquid nitrogen for cooling on a TA-DSC25. Conductivity of the electrolytes with different additive concentrations was obtained using a conductivity meter (Rex Electric Chemical, DDS-307A). In-situ optical microscope video and images were obtained from a YP510TR optical microscope (Suzhou

Yueshi Precision Instrument Co. LTD). Galvanostatic Zn plating was conducted at a constant current density of 5 mA cm^{-1} for a fixed time of 40 mins using an electrochemical workstation (CHI660E, Chenhua, Shanghai).

Computation methods

Molecular dynamics simulations were performed using the GRMOACS 2020.6 package, and structures were visualized with VMD software. The molecules were mixed in a cubic box with periodic boundary conditions using the PACKMOL package.[1-3] The number of the molecules is shown in the table:

System	H$_2$O	Zn(BF$_4$)$_2$	DME
ZBFD	414	69	356
Zn(BF$_4$)$_2$	2622	69	—

In this work, the Generation Amber Force Field (GAFF) was selected as it is suitable for investigating various small organic molecules. The Sobtop code was used to generate the necessary force field parameters for the simulation systems. The partial charges on atoms were obtained using the restrained electrostatic potential (RESP) method and calculated with Multiwfn software.[4]

Before starting the MD simulation, the initial configurations were relaxed using a conjugate gradient minimization scheme. The step size for the conjugate gradient minimization scheme was set to 0.01 nm, and the cycle was set to 5000 steps. The minimization force was considered converged when it was less than 100 kJ·mol^{-1}·nm^{-1}. Van der Waals interaction was calculated using the cut-off method, while atomic electrostatic interaction was calculated by PME (particle mesh Ewald) with both the cut-off and PME distances set to 1.0 nm.[5] The system was then equilibrated with a pressure of 1.0 bar to attain the desired density using the Berendsen and V-rescale methods for pressure and temperature control, respectively. The time constant was 1.0 ps, and the compressibility was 4.5×10^{-5} bar^{-1}. Equilibrium was performred for 5

ns for all systems with a time-step of 0.001 ps. Finally, production was run for 50 ns, with pressure control switched to the Parrinello-Rahman method. To impose constraints on hydrogen bonds, the LINCS (Linear Constrain Solver) algorithm was used. [6]

Binding Energies were calculated using the Gaussian (G09) program at the B3LYP-D3(BJ)/6-311+G** level for neutral molecules and cations and B3LYP-D3(BJ)/6-311+G** level for anions. The implicit universal solvation model based on Solute Electron Density (SMD)[7] with a dielectric constant of water was employed to investigate the influence of the solvents. The binding energies (E_B) were calculated using the following equation:

$$E_B = E_{com} - \sum E_{fra}$$

where E_{com} is the total energy of the complex, E_{fra} is the energy of each fragment.

The Gibbs free energy of solvated structures and interaction between Zn crystal and molecules were calculated using the DMol3 code in the Material Studio software, employing the Perdew-Burke-Ernzerhof (PBE) generalized gradient approximation (GGA) and double-numerical properties plus polarization (DNP) functions as the base set.[8] The convergence tolerance for energy, force, and displacement was set at 10^{-6} Ha, 0.004 Ha/Å, and 0.005 Å, respectively.[9] To avoid the influence of periodic adjacent layers, a vacuum layer of 15 Å was used in the direction of vertical substrate plane.[10]

The Gibbs free energies (ΔG_f) were calculated using the following equation:

$$\Delta G_f = G_{com} - \sum G_{fra}$$

The absorbed energy between Zn slab and different molecules was defined using the following equation:

$$E_{aborb} = E_{Zn-slab+molecules} + E_{Zn-slab} - E_{molecules}$$

2. Figure and tables
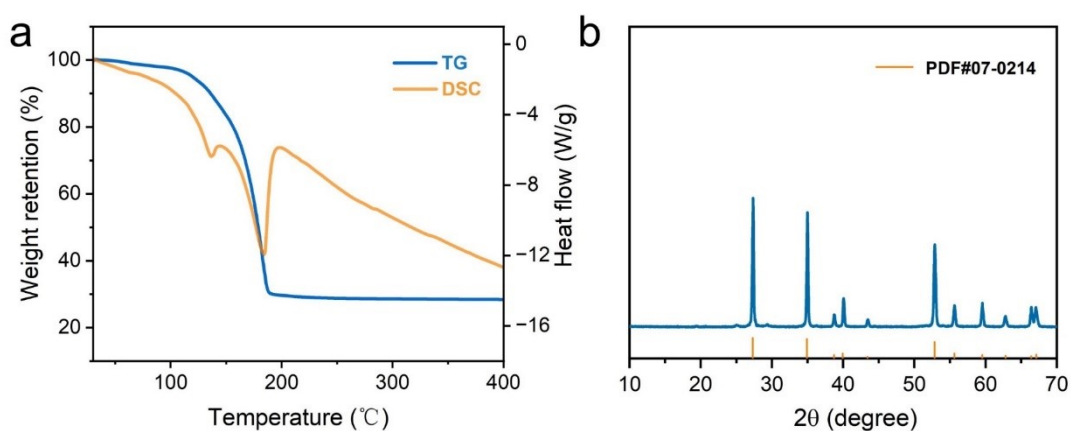
Fig. S1 (a) TGA and DSC curves of the purchased hydrated $Zn(BF_4)_2$ salt from 25 °C to 400 °C. The weight

loss before 200 °C is due to both the release of water and the decomposition of $Zn(BF_4)_2$. (b) The XRD

patten of the decomposition product of the hydrated $Zn(BF_4)_2$ salt, which indicates that the residual solid

after TGA is ZnF_2.
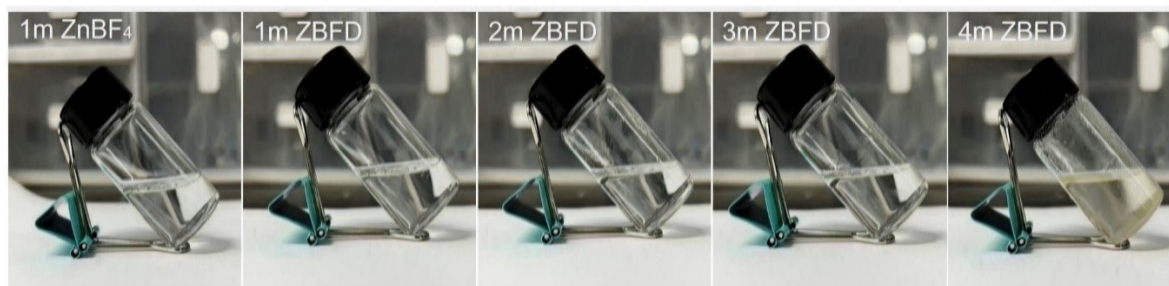
**Fig. S2** Optical photographs of different electrolytes at room temperature.
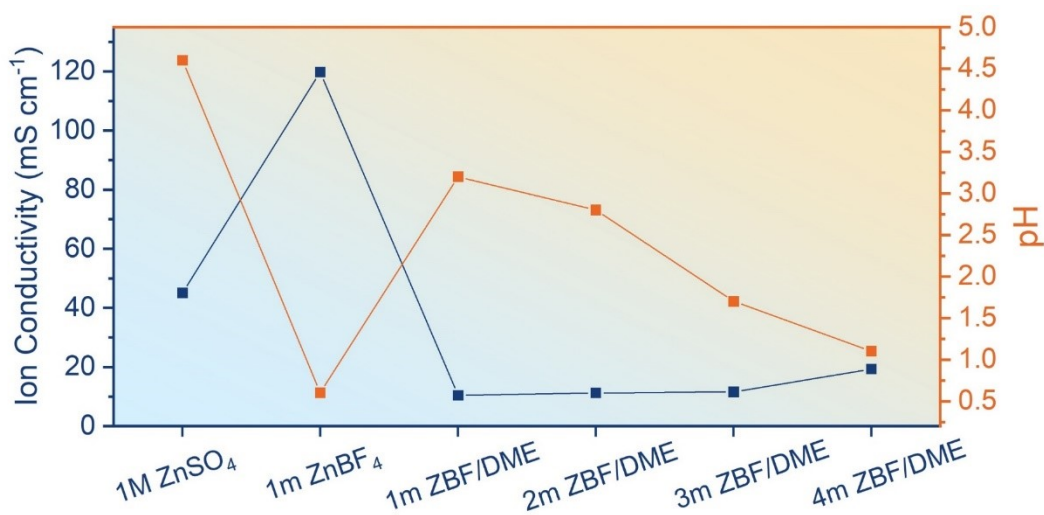
Fig. S3 Ion conductivity and pH of different electrolytes at room temperature.

The 1m ZnBF$_4$ electrolyte exhibited a high ionic conductivity of 119.8 mS cm^{-1}, which surpassed that of the ZnSO$_4$ electrlyte (45.2 mS cm^{-1}). However, this high conductivity is due to the hydrolysis of BF$_4^-$ to produce more H$^+$, which results in a sharp decrease in the pH of the electrolyte, making it unfavorable for metal electrodes. In contrast, the eutetic electrolyte, which inhibits hydrolysis, exhibits a significicnat decrease in ionic conductivity.
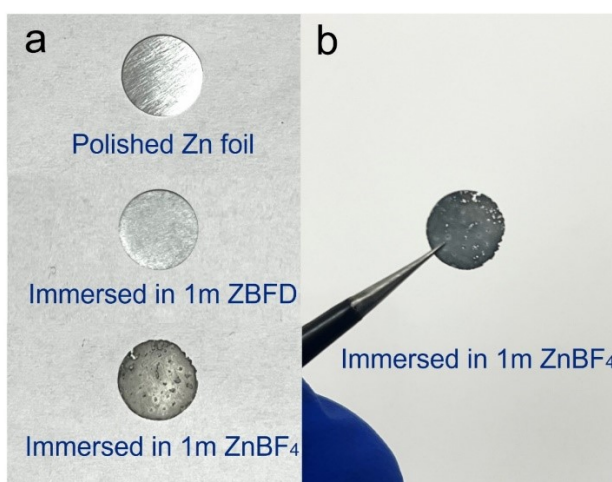
Fig. S4 Comparative images of the Zn foil before and after immersion in the Zn(BF$_4$)$_2$ electrolyte.

After three days of immersion in the electrolyte, the Zn foil became dark and showed holes due to severe corrosion.
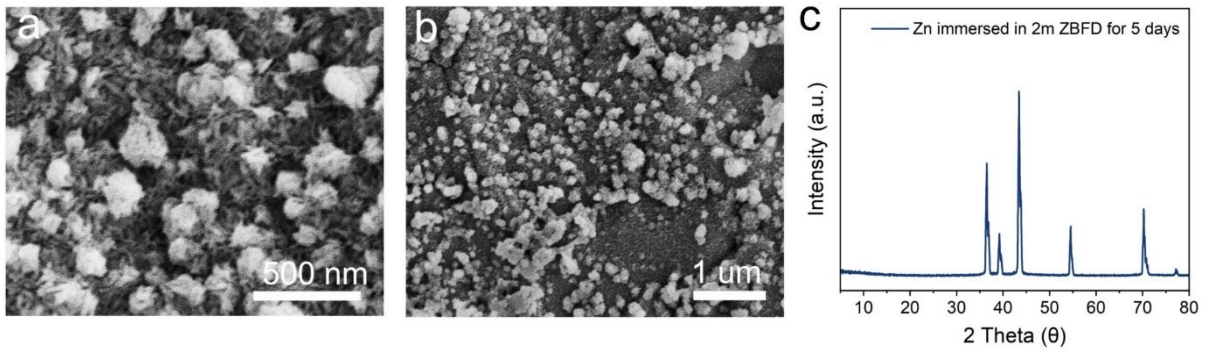
Fig. S5 Morphology and structure of the suface of Zn foil after immersion in ZBFD electrolyte.
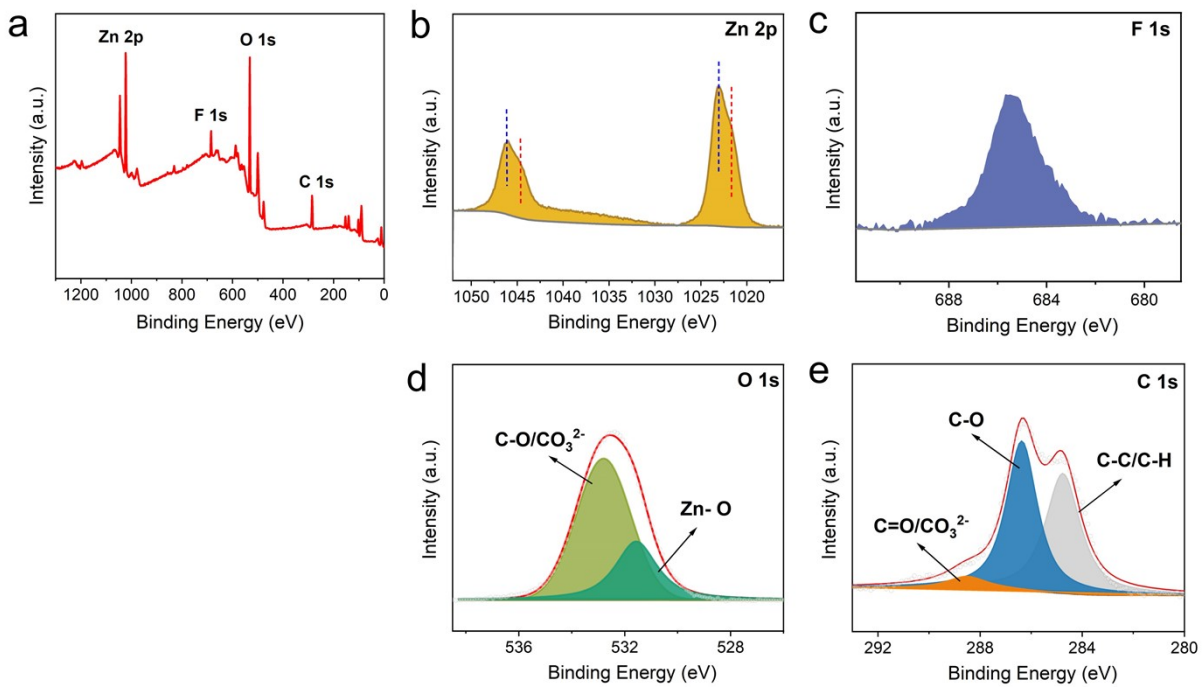
Fig. S6 XPS pattens of the suface of Zn foil after immersion in ZBFD electrolyte.
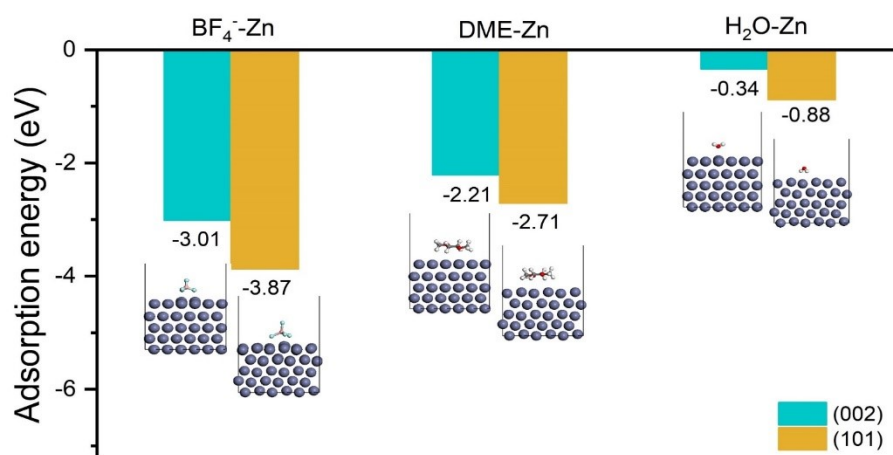
Fig. S7 Adsorption energy of each component in the electrolyte with different crystal planes of Zn.
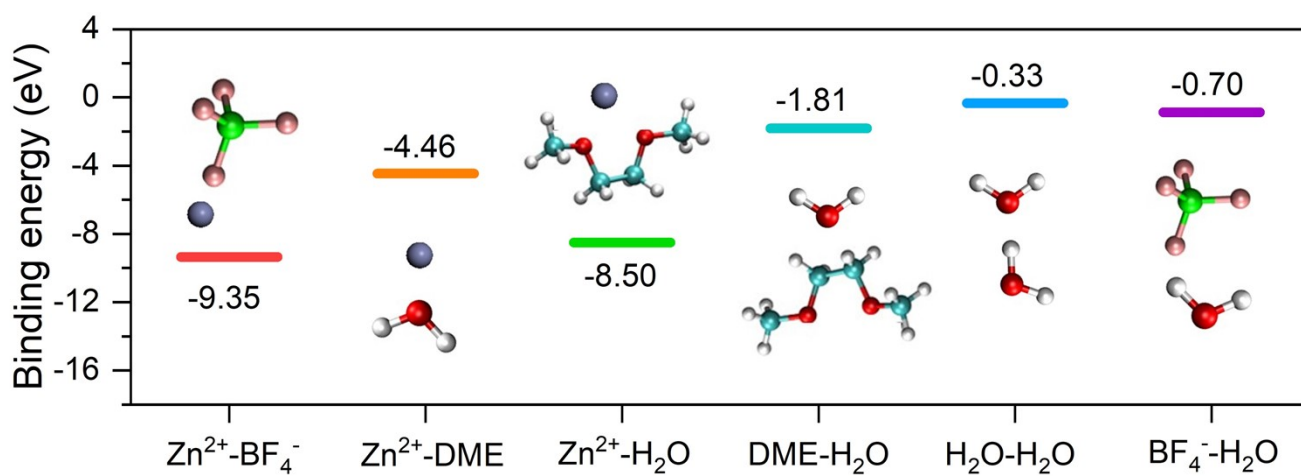
Fig. S8 Binding energy between different components in ZBFD electrolyte calculated by density functional theory.
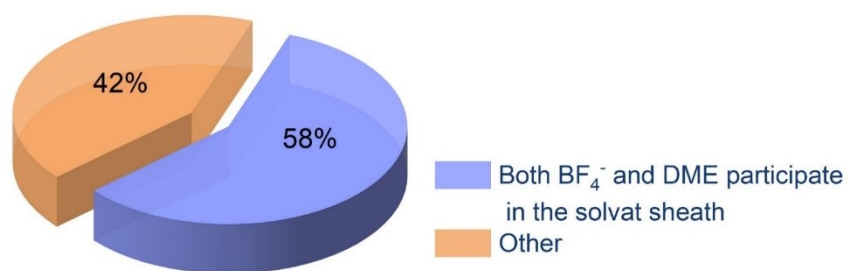
Fig. S9 Distribution of the BF_4^- and DME participating solvation structure.
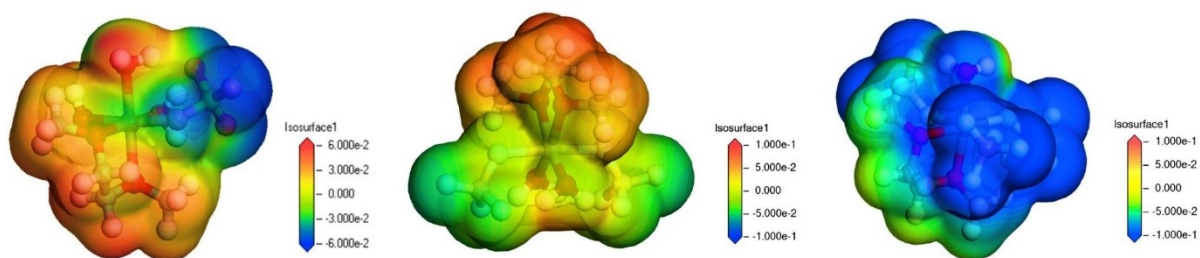
Fig. S10 Electrostatic potential mapping of several solvated structures.

Table S1 Gibbs free energy and bond strength for different solvated structures.

Solvated structure	Gibbs Free Energy ΔG (eV)	Bonding Strength ΔE (eV)
$[Zn(DME)(H_2O)_3]^{2+}\cdot(BF_4^-)$	-3.50	1.29
$[Zn(DME)(H_2O)_2]^{2+}\cdot(BF_4^-)_2$	-3.68	1.37
$[Zn(DME)(H_2O)]^{2+}\cdot(BF_4^-)_3$	-3.47	1.23
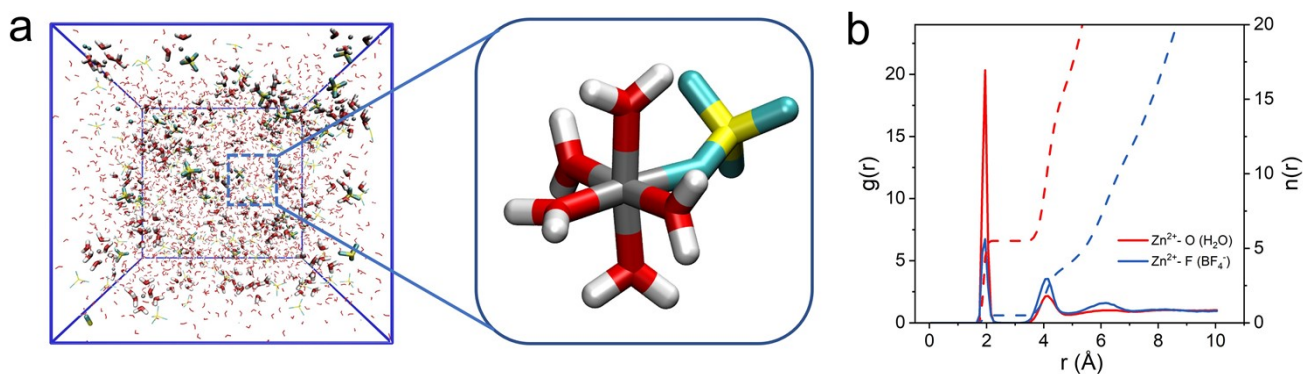
Fig. S11 (a) 3D snapshots of $Zn(BF_4)_2$ electrolyte obtained from MD simulations and partially enlarged snapshots of the solvation structure of Zn^{2+}. (b) The radial distribution functions and coordination number of Zn^{2+}-O and Zn^{2+}-F collected from MD simulations.

Fig. S11 shows a 3D snapshot where BF_4^- and H_2O molecules jointly participate in the Zn^{2+} solvent shell. The radial distribution function indicates that these species have an average coordination distance of about 0.2 nm, with average coordination numbers of 5.5 and 0.5 for H_2O and BF_4^-, respectively.
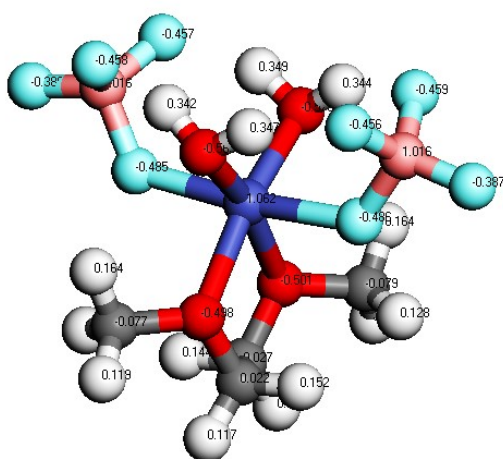
	Zn^{2+}	DME	BF_4^-	H_2O
Free	2.00	0	-1.00	0
Bond	1.06	0.24	-0.77	0.12

Fig. S12 The charge distribution of each element in the solvation structure of $[Zn(DME)(H_2O)_2]^{2+}\cdot(BF_4^-)_2$.

Free DME

Bond DME
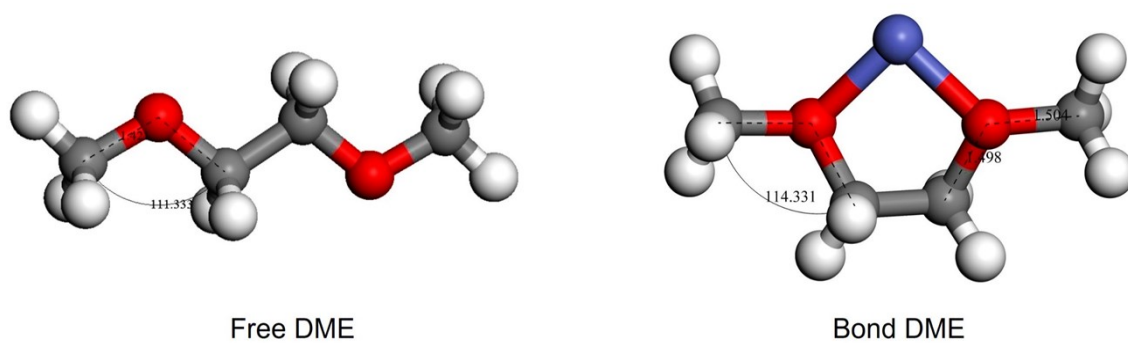
**Fig. S13** Configuration characteristics of DME molecules before and after coordination.
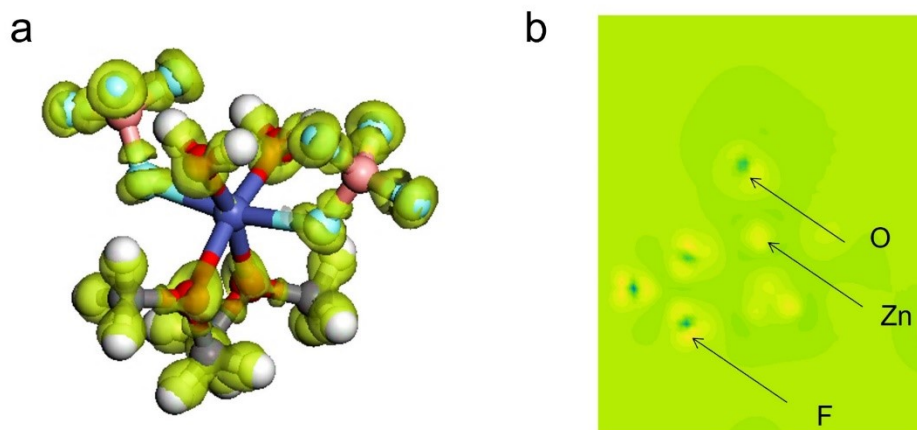
Fig. S14 (a) Charge density difference for $[Zn(DME)(H_2O)_2]^{2+}\cdot(BF_4^-)_2$ and (b) the corresponding 2D sectional contour map.
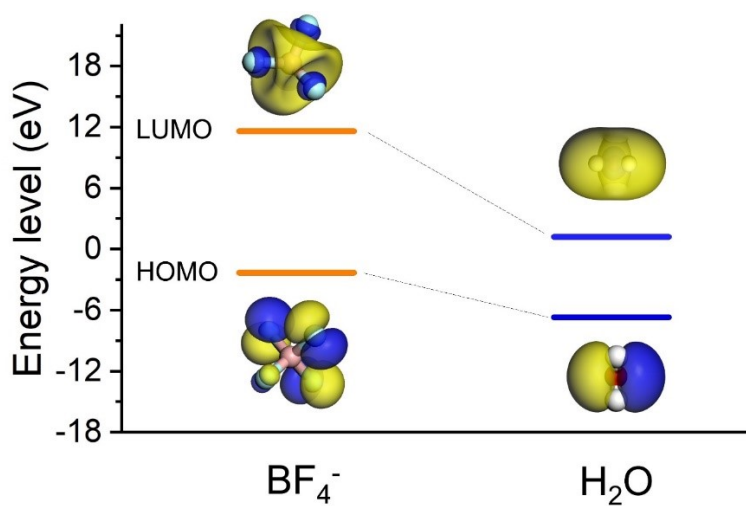
Fig. S15 HOMO/LUMO energy levels of BF_4^- and H_2O.
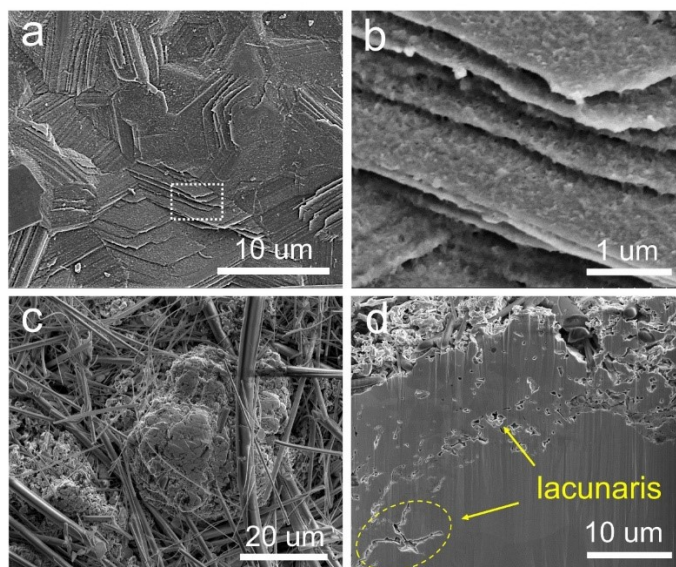
Fig. S16 SEM images of the ZMA after cycling in (a,b) ZBFD electrolyte and (c) ZnSO$_4$ electrolyte. (d)

Cross section of the deposited Zn foil in ZnSO$_4$ electrolyte.
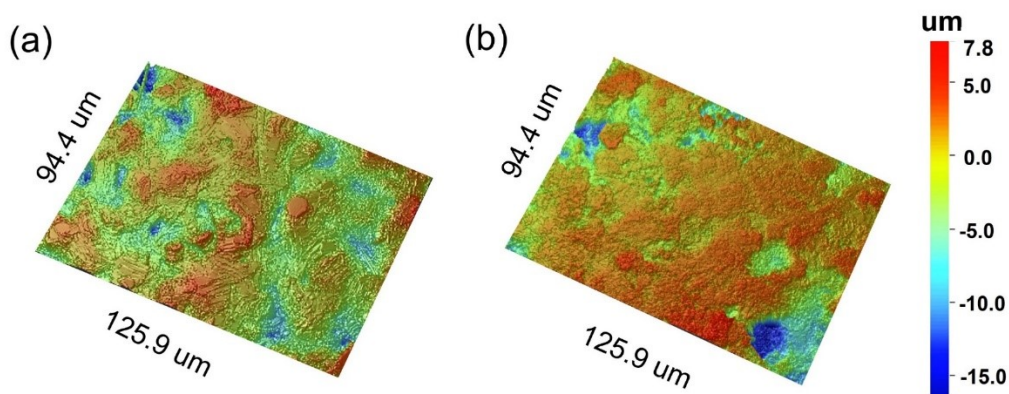
Fig. S17 Optical surface profilometry images of the ZMA deposited in (a) ZBFD electrolyte and (b) ZnSO$_4$

electrolyte.
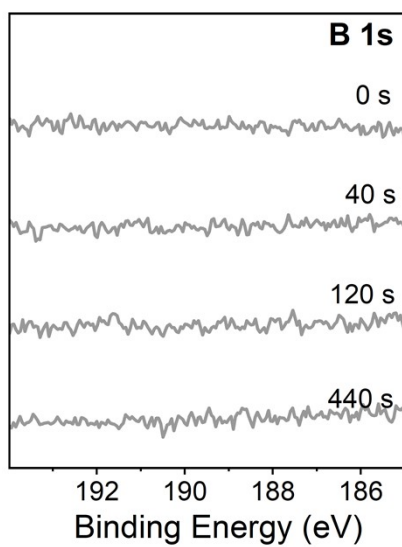
Fig. S18 The B 1s XPS spectra of a Zn electrode with different sputtering times. The electrode was obtained from a Zn//Zn symmetrical cell that had been cycled 50 times.
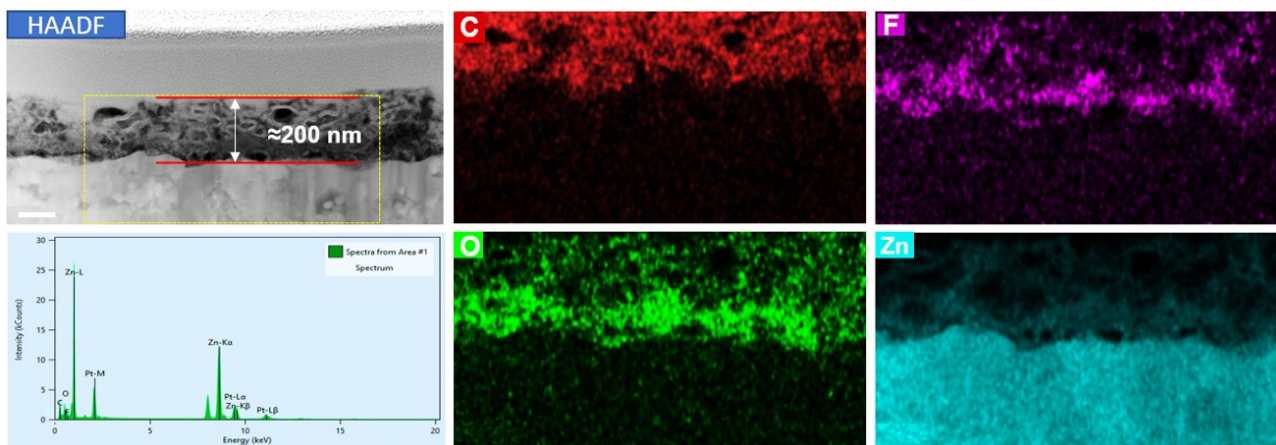
Fig. S19 A cross-sectional HRTEM image and corresponding elemental distribution of a Zn electrode after 200 cycles. The scale bar is 100 nm. Note: The cross-section of the SEI layer after cycling is precisely observed using FIB-TEM. The SEI layer thickness remained within 200 nm, and the structure was consistent with previous observations, with a lower layer composed of dense particles and an upper composed of porous channels. The element distribution analysis showed that C was mainly distributed in the upper layer, while F was distributed in the bottom layer. These results indicate that the structure and composition of the hybrid SEI layer did not change significantly after cycling.
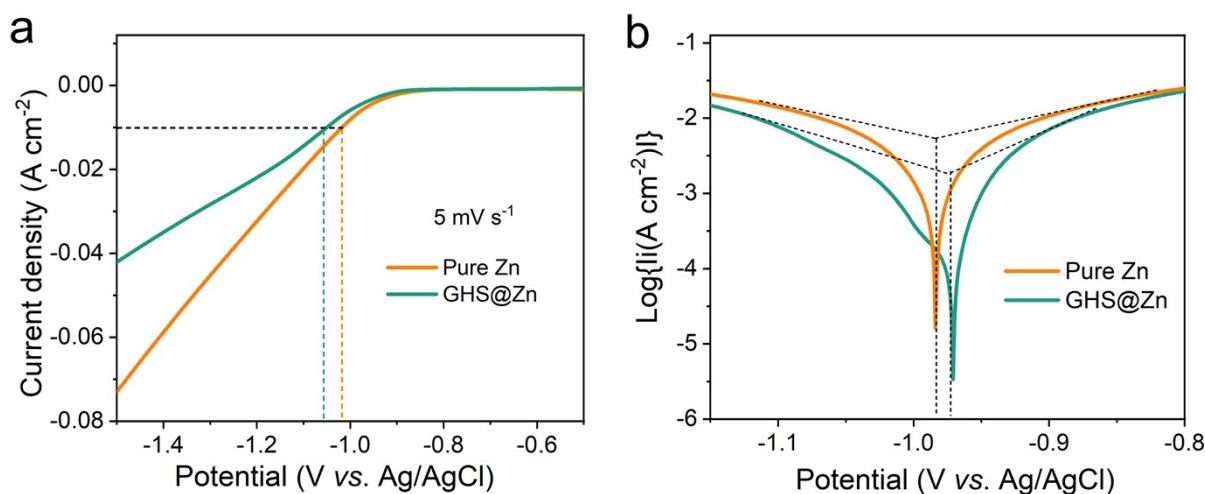
Fig. S20 (a) LSV curves and (b) Tafel plots of the pure Zn and GHS@Zn foils measured in the ZnSO$_4$ electrolyte.

GHS@Zn has a lower onset potential of HER (-1.068 V) compared to bare Zn (-1.016 V), indicating significant suppression of electrochemical reduction of H_2O (HER) by the hybrid SEI layer. Meanwhile, the GHS@Zn electrode exhibited a more positive corrosion potential and lower corrosion current, indicating that the corrosion reaction was effectively suppressed by the hybrid SEI layer.
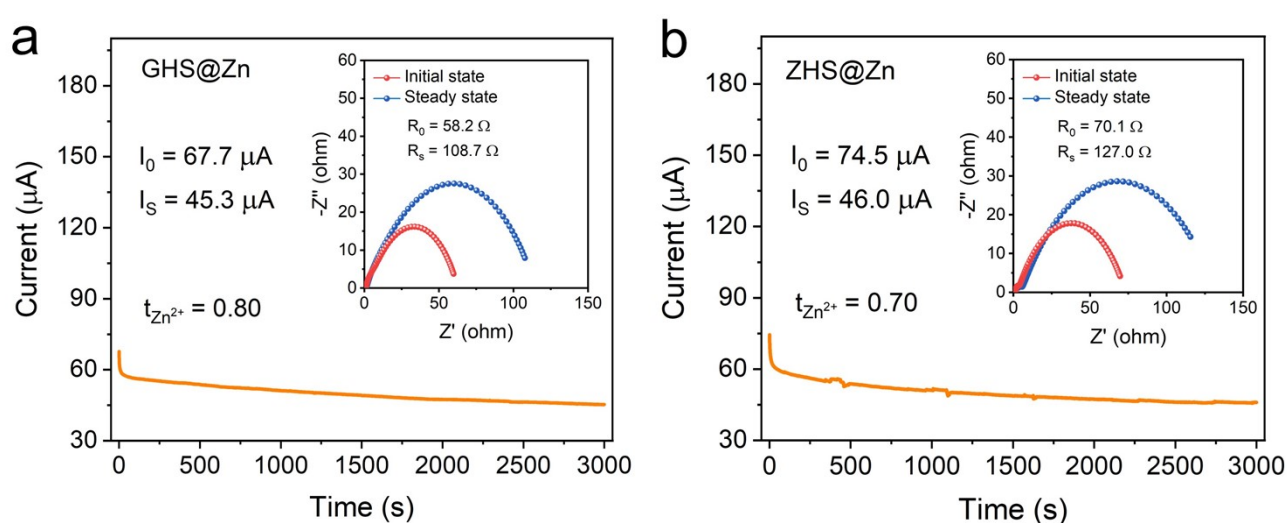

Fig. S21. Current-time plots of (a) GHS@Zn‖GHS@Zn and (b) ZHS@Zn‖ZHS@Zn symmetric cells after polarization at a constant potential (10 mV) for 3000 s. The insets present the impedance spectra before and after polarization.

The transference number of ($t_{zn^{2+}}$) was calculated according to the following equation:

$$t_{zn^{2+}} = \frac{I_s(\Delta V - I_0 R_0)}{I_0(\Delta V - I_s R_s)}$$

Where ΔV is the applied polarization voltage (10 mV), I_0 and R_0 are the initial current and resistance, and I_s and R_s are the steady-state current and resistance, respectively.
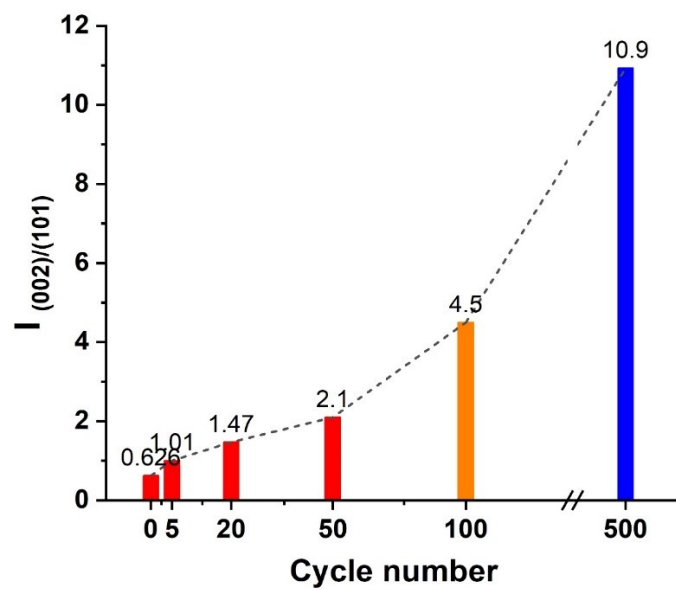
Fig. S22 The relative peak intensity of (002) over (101) [$I_{(002)/(101)}$] in XRD patterns of the ZMA with different cycles.

Table S2 Intensity obtained from a textured sample I(hkl) and the intensity of the standard oriented sample I_0(hkl) of Zn anodes.

Intensity	(002)	(100)	(101)	(102)	(103)	(110)	(004)
I_0	39.6	23.3	100.0	14.4	15.2	10.0	2.3
I- 0th	5681	2291	9081	1859	2279	737	245
I-5th	6367	1386	6329	1612	1924	468	299
I- 20th	7493	1080	5094	1287	1778	394	302
I-50th	10524	1022	5011	1166	1416	317	262
I-100th	12896	733	2866	844	1302	364	594
I-500th	20056	388	1835	792	1668	180	520

The relative texture coefficients (RTCs) for each Zn lattice plane were calculated using the following formular,[2]

$$RCT_{(hkl)} = \frac{I_{(hkl)}/I_{0(hkl)}}{\sum (I_{(hkl)}/I_{0(hkl)})}$$

where I(hkl) is the intensity obtained from the textured sample, and I0(hkl) is the intensity of the standard-oriented sample.
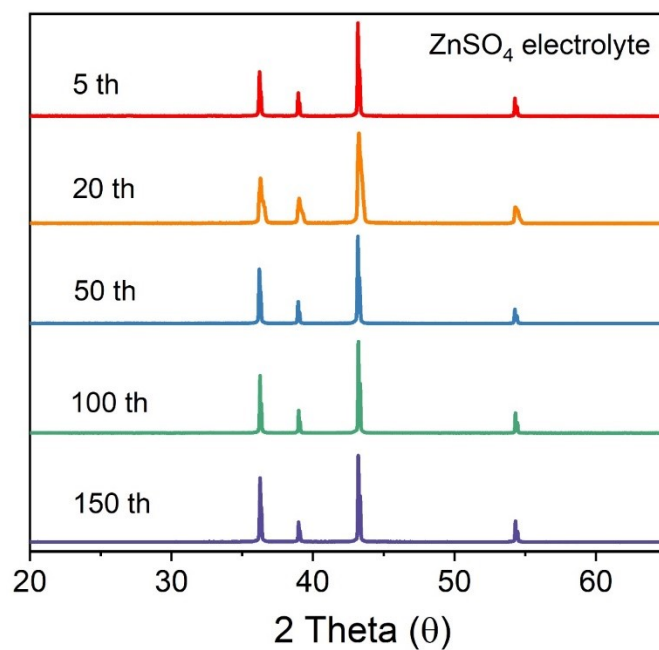
**Fig. S23** XRD patterns of ZMA after different cycles in $ZnSO_4$ electrolyte.

In $ZnSO_4$ electrolyte, as-deposited Zn always exhibits a strong diffraction peak representing the (001) crystal plane, indicating disordered deposition of Zn^{2+}. This irregular deposition can induce a tip effect, leading to uncontrolled growth of Zn dendrites.
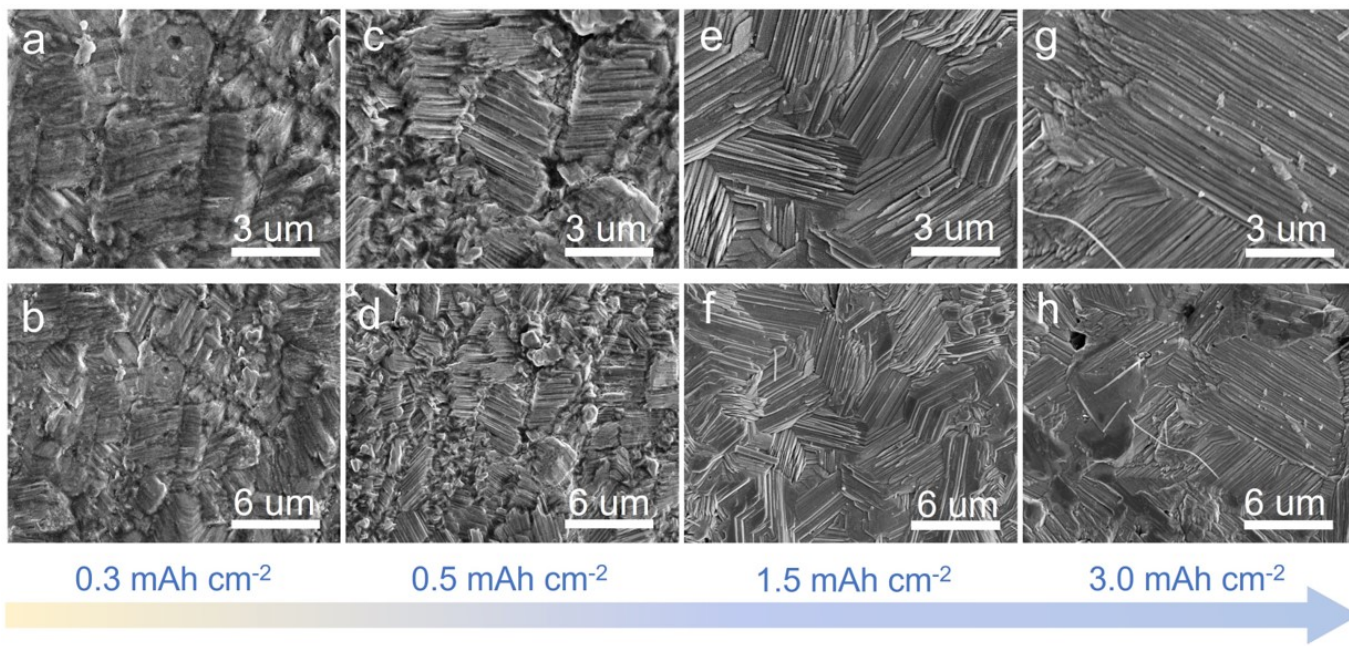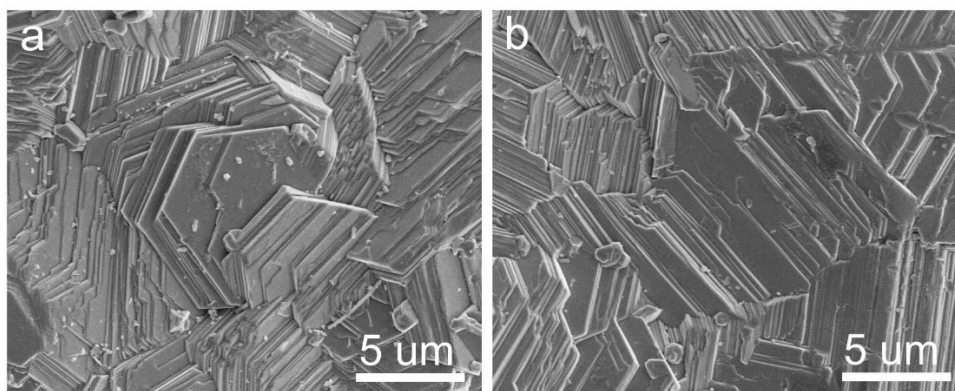
Fig. S24. The morphology evolution of the Zn anode during the platting process with a current density of 5 mA cm^{-2}.
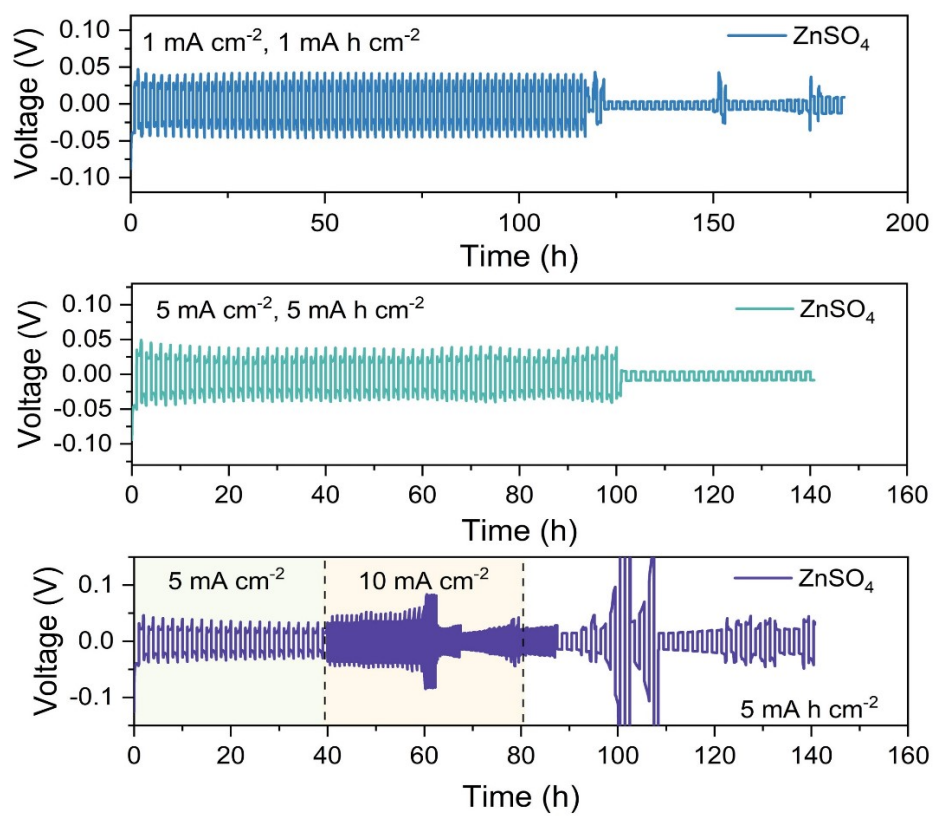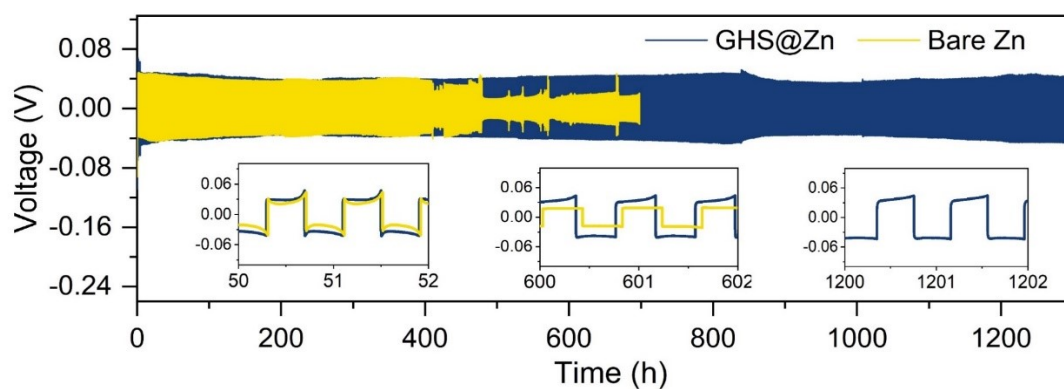
Fig. S25 Electrochemical performance of Zn//Zn symmetrical cells using ZnSO$_4$ electrolyte.
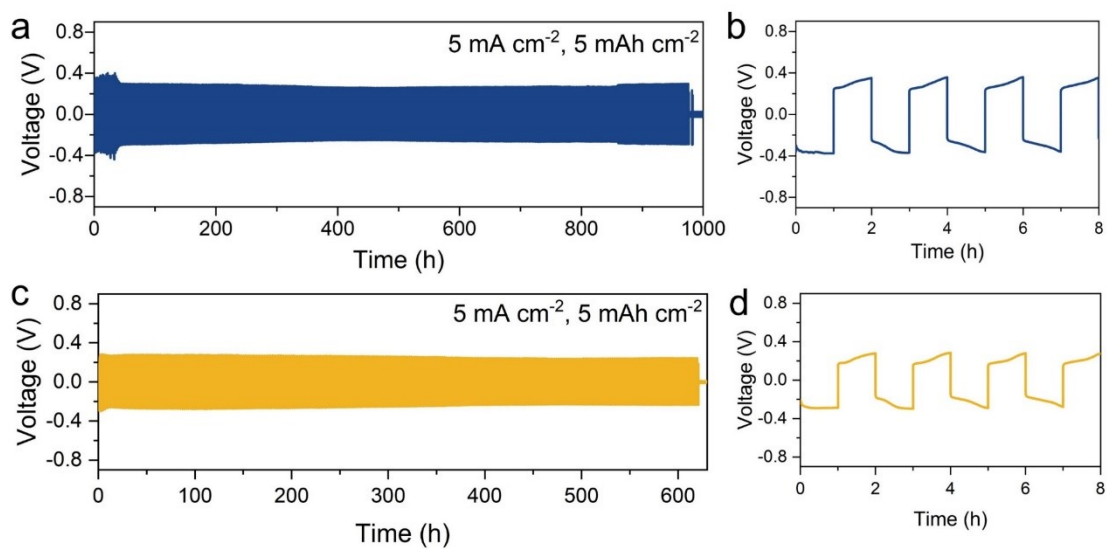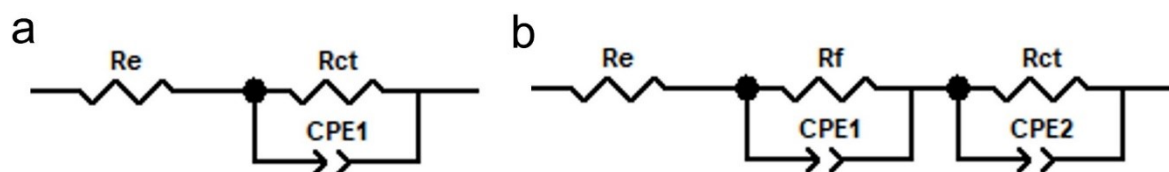
Fig. S26 Cycling performance of cells using electrolyte with (a) 1m ZBFD electrolyte and (b) 3m ZBFD electrolyte.

Fig. S27 The SEM images of the ZMA cyced in (a) 1m ZBFD electrolyte and (b) 3m ZBFD electrolyte.

Fig. S28 The cycling stability of GHS@Zn and bare Zn foil in ZnSO₄ electrolyte. The GHS@Zn was obtained from the symmetrical cell using ZBFD electrolyte after 30 cycles.
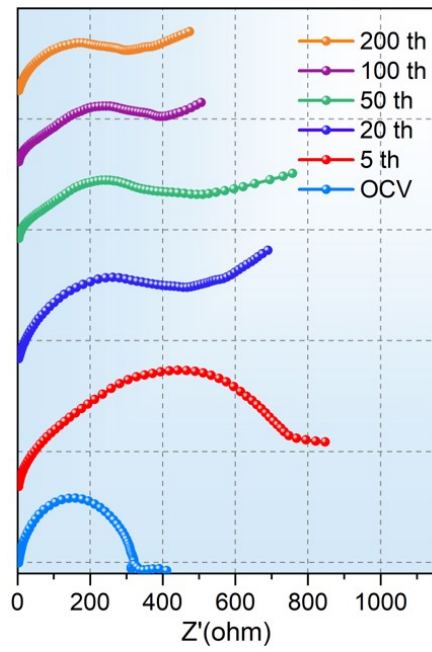

Fig. S29 Equivalent circuit diagram used to fit the impedance of the (a) initial state and (b) operating state of the cells.
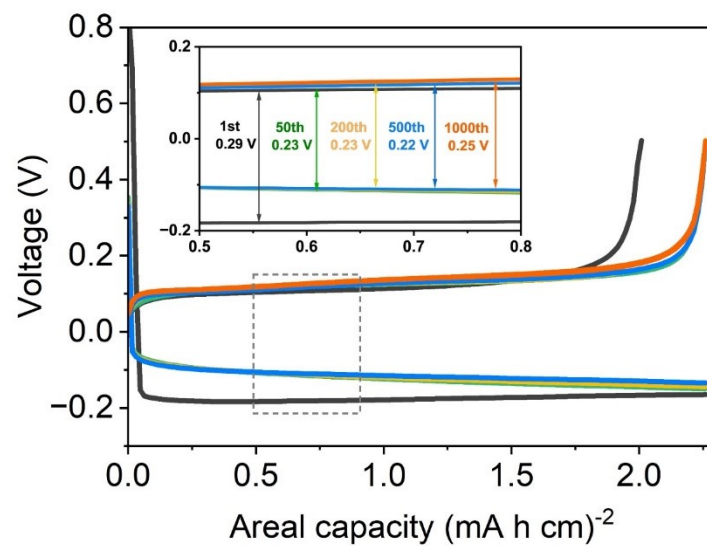
Table S3 Interfacial impedance of the cell in different states.

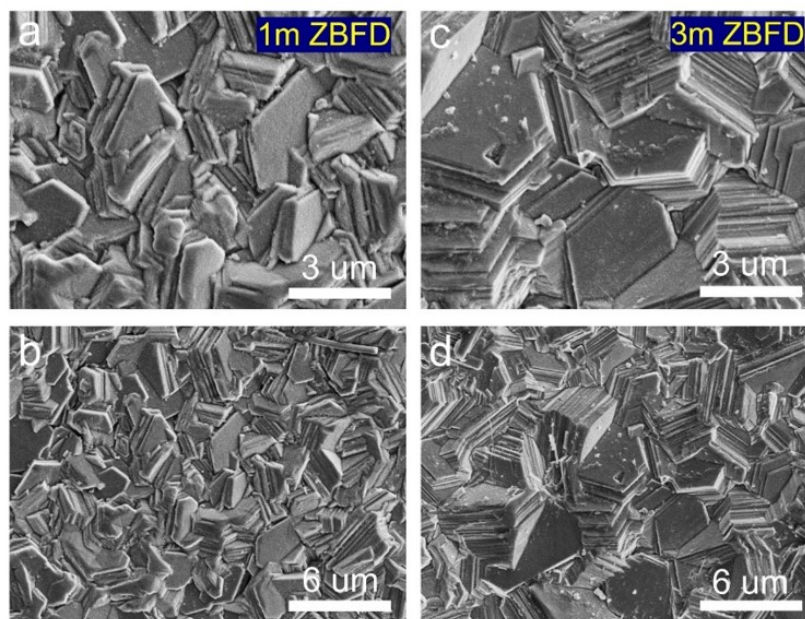| Intensity	OCV	5 th	20 th	50 th	100 th	200 th
R_{SEI}	/	131.0	66.4	65.1	57.2	50.3
Rct	350.2	612.3	380.3	372.9	352.4	273.7

**Fig. 30** The original Nyquist plots of the Zn symmetrical cells after different cycles.

Fig. S31 The voltage profiles of the Zn//Cu cell with ZBFD electrolyte.

Fig. S32 The morphology of Cu electrodes deposited in (a, b) 1m and (c, d) 3m ZBFD electrolyte under

test conditions of 5 mA cm^{-2} and 2 mA h cm^{-2}.
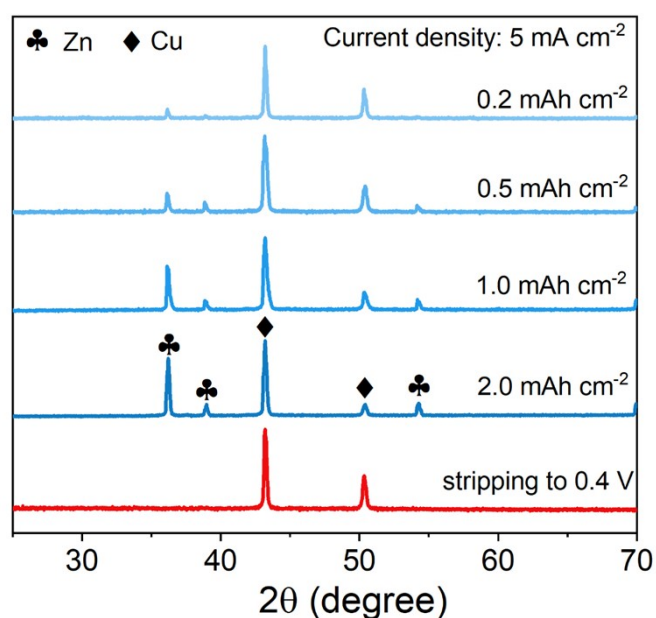

Fig. S33 XRD patterns of Cu electrodes at several specific deposition capacities in ZnSO$_4$ electrolyte. With

increasing deposition capacity, the characteristic peak of Zn metal is gradually enhanced, but no signal of
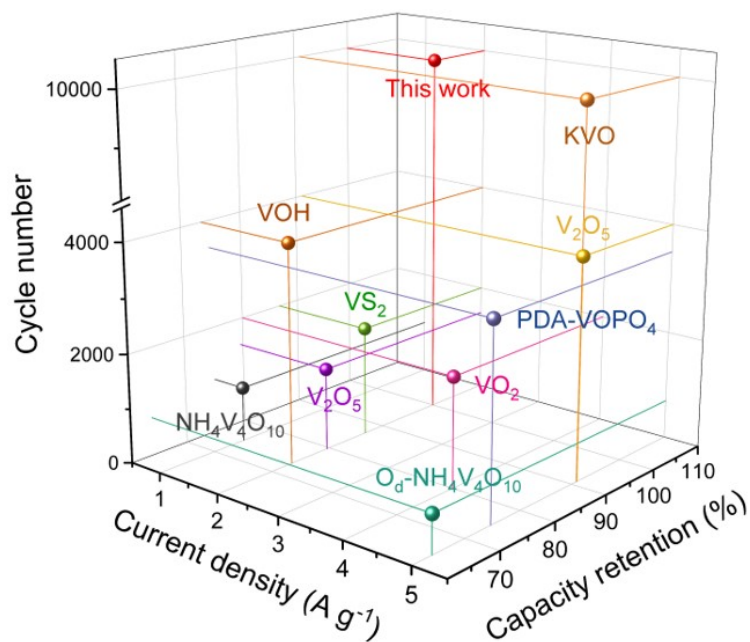
the Zn-Cu alloy is observed.
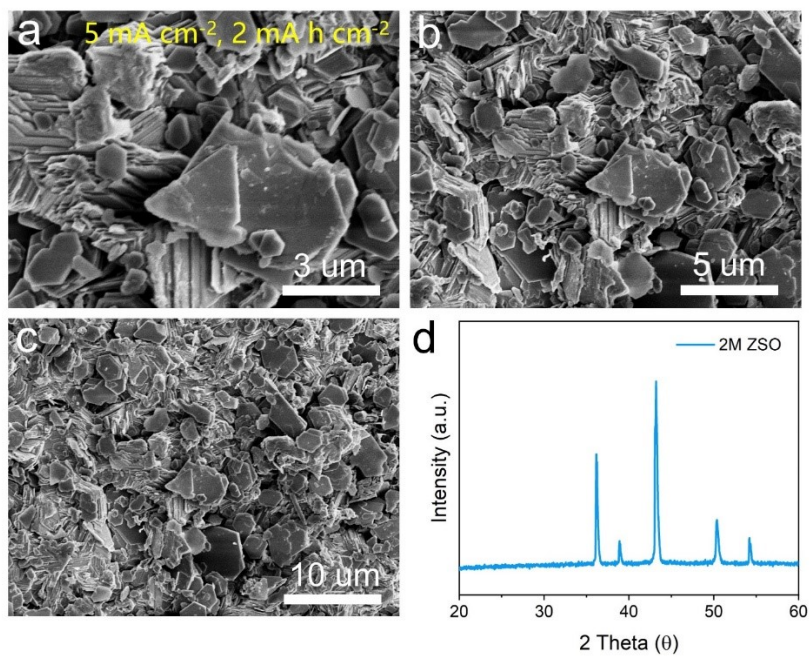
Fig. S34 The morphology and structure of a Cu electrode deposited in 2M ZnSO$_4$ electrolyte.
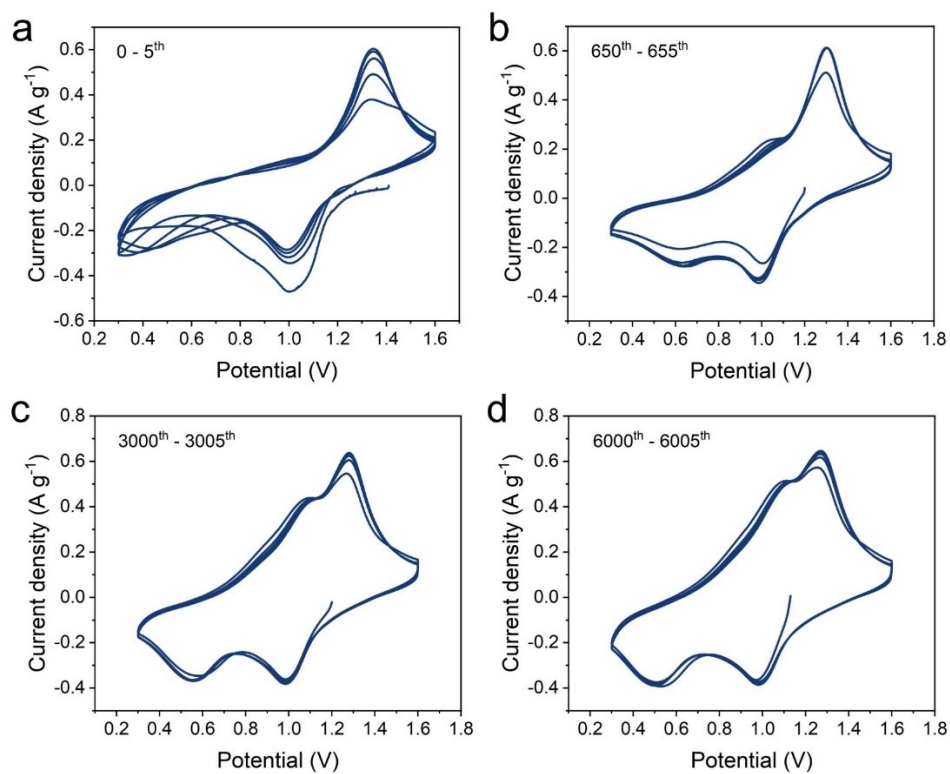
Fig. S35 CV curves for the Zn//V$_2$O$_5$ full cells at different cycles.
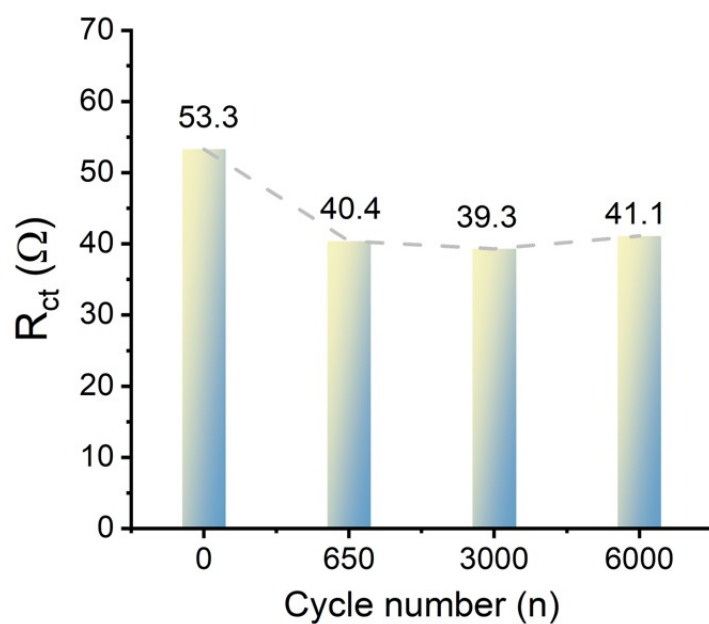
Fig. S36 Corresponding charge transfer impedance values (R_{ct}) of the Zn//V_2O_5 full cells after different cycles.

Fig. S37 Comparison of the cycling performance between the present Zn//V_2O_5 with ZBFD electrolyte and the previously reported full cells with different cathodes.
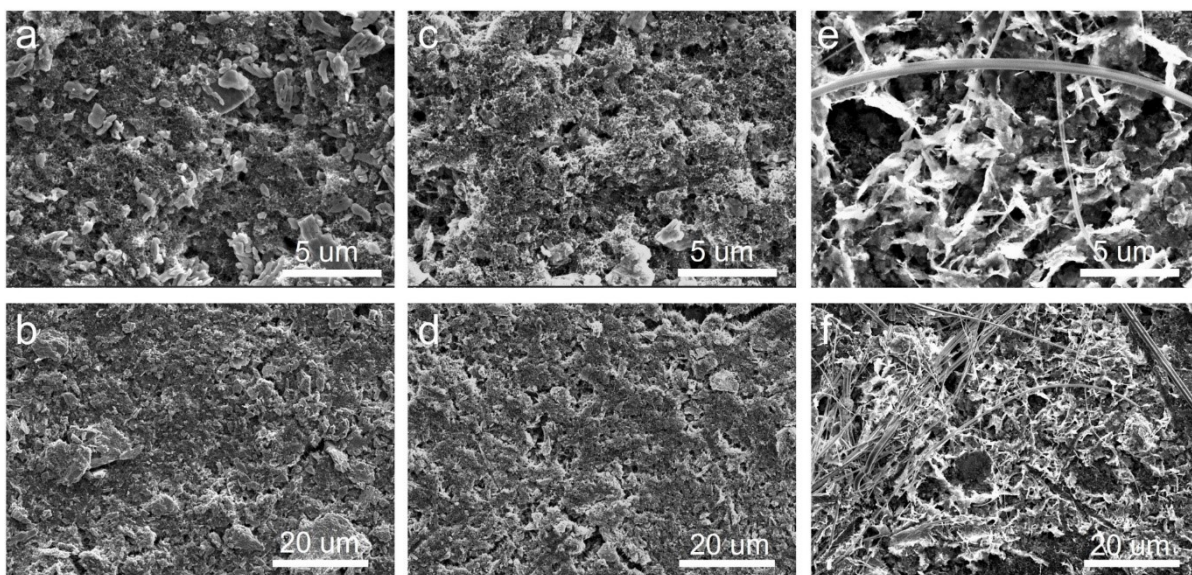
Fig. S38 Morphology of the V_2O_5 electrodes (a,b) before cycling and after cycling in (c,d) ZBFD electrolyte and (e,f) $ZnSO_4$ electrolyte.
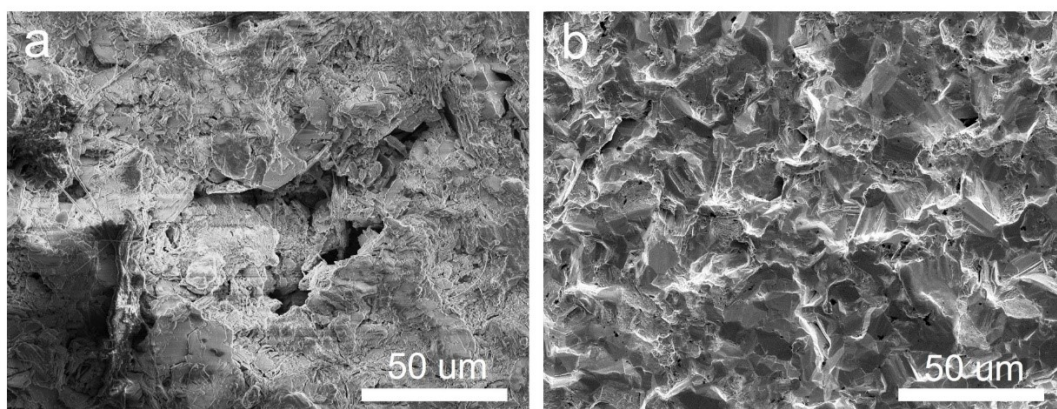
Fig. S39 The SEM images of ZMA after cycling in $Zn//V_2O_5$ full cells using (a) $ZnSO_4$ electrolyte and (b) ZBFD electrolyte.
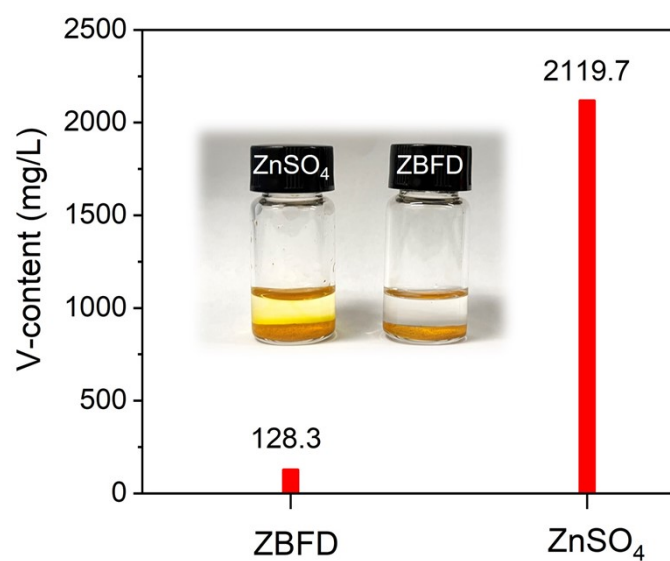
Fig. S40 The V-content of the different electrolytes (by ICP-OES) after soaking with V_2O_5. The insets are optical images of the V_2O_5-electrolytes systems (15 mg V_2O_5 was immersed in 5 mL of the electrolytes).
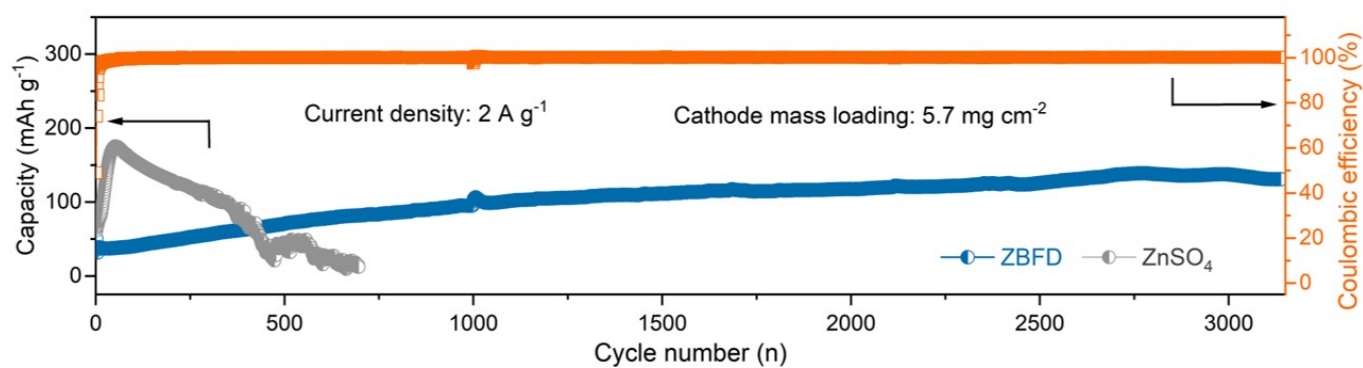
Fig. S41 Long-term cycling stability of full cells assembled using ultra-thin Zn anode (20 μm) and V_2O_5 cathode with high mass loading (5.7 mg cm^{-2}) in different electrolytes.

Table S4 Comparison of the cycling stability of Zn-Zn symmetric cells with previous reports.

Modification Strategies	Cycling Stability of Zn//Zn cells	Lifespan	Cumulative capacity (mAh cm^{-2})	References
This work	1 mA cm^{-1}, 1 mAh cm^{-2}	3200 h	1600	/
	5 mA cm^{-1}, 5 mAh cm^{-2}	2230 h	5575	
TBA$_2$SO$_4$ additive	10 mA cm^{-1}, 2 mAh cm^{-2}	400 h	2000	11
AEC coating	8.85 mA cm^{-1}, 8.85 mAh cm^{-2}	250 h	1106.25	12
TMA additive	5 mA cm^{-1}, 2.5 mAh cm^{-2}	500 h	1250	13
Glucose additive	5 mA cm^{-1}, 5 mAh cm^{-2}	300 h	750	14
Anion induced texturing Zn	10 mA cm^{-1}, 2 mAh cm^{-2}	200 h	1000	15
BN layer	10 mA cm^{-1}, 10 mAh cm^{-2}	350 h	1750	16
Ethylene glycol (EG)	2.0 mA cm^{-1}, 1.0 mAh cm^{-2}	140 h	140	17
LiCl additive	5.0 mA cm^{-1}, 1.0 mAh cm^{-2}	170 h	425	18
cation additive (Ce^{3+}, La^{3+})	1.0 mA cm^{-1}, 1.0 mAh cm^{-2}	400 h	200	19
	5.0 mA cm^{-1}, 1.0 mAh cm^{-2}	700 h	1750	
Zn(H$_2$PO$_4$)$_2$ additive	1.0 mA cm^{-1}, 1.0 mAh cm^{-2}	1200 h	600	20
	1.0 mA cm^{-1}, 5.0 mAh cm^{-2}	800 h	400	
Acetamide additive	0.1 mA cm^{-1}, 0.1 mAh cm^{-2}	1500 h	75	21
Diethyl ether additive	0.2 mA cm^{-1}, 0.2 mAh cm^{-2}	250 h	25	22
Hydrated eutectic electrolytes	0.05 mA cm^{-2}, 0.5 mAh cm^{-2}	800h	4	23
	0.2 mA cm^{-2}, 2 mAh cm^{-2}	400 h	40	

3D carbon nanotube	5.0 mA cm^{-2}, 2.5 mAh cm^{-2}	110 h	275	24
	2.0 mA cm^{-2}, 2.0 mAh cm^{-2}	200 h	200	
3D-Zn in TBA electrolyte	5.0 mA cm^{-2}, 5.0 mAh cm^{-2}	160 h	400	25
Gel electrolyte	5.0 mA cm^{-2}, 5.0 mAh cm^{-2}	500 h	1250	26
Na$_4$EDTA additive	5.0 mA cm^{-2}, 2.0 mAh cm^{-2}	2000 h	5000	27
DOTf additive	4.0 mA cm^{-2}, 4.0 mAh cm^{-2}	400 h	800	28
Fluoroethylene carbonate (FEC) additive	4.0 mA cm^{-2}, 1.0 mAh cm^{-2}	1000 h	2000	29
Molecular sieves (MCM41)	1.0 mA cm^{-2}, 1.0 mAh cm^{-2}	1750 H	875	30
Metal-organic complexes (Zn-PA@Zn)	5.0 mA cm^{-2}, 2.5 mAh cm^{-2}	1700 h	4250	31
	0.5 mA cm^{-2}, 0.25 mAh cm^{-2}	2000 h	500	
AIN/Ag protective layer	1.0 mA cm^{-2}, 1.0 mAh cm^{-2}	2600 h	1300	32
	2.0 mA cm^{-2}, 2.0 mAh cm^{-2}	500 h	500	

References:

1. M.J. Abraham, T. Murtola, R. Schulz, S. Páll, J.C. Smith, B. Hess and E. Lindahl, *SoftwareX*. 2015, **1-2,** 19-25.

2. W. Humphrey, A. Dalke and K. Schulten, *J Mol Graph*. 1996, **14**, 33-38.

3. J. Wang, R.M. Wolf, J.W. Caldwell, P.A. Kollman and D.A. Case, *J. Comput. Chem.* 2004, **25**, 1157-1174.

4. T. Lu and F. Chen, *J. Comput. Chem.* 2012, **33**, 580-592.

5. P. Li, B.P. Roberts, D.K. Chakravorty and K.M. Merz, *J. Chem. Theory Comput*. 2013, **9**, 2733-2748.

6. B. Hess, H. Bekker, H.J.C. Berendsen and J.G.E.M. Fraaije, *J. Comput. Chem.* 1997, **18**, 1463-1472.

7. A.V. Marenich, C.J. Cramer and D.G. Truhlar, *The Journal of Physical Chemistry B*. 2009, **113***, 6378-6396.

8. L. Chen, X. Chen, C. Duan, Y. Huang, Q. Zhang and B. Xiao, *Physical chemistry chemical physics.,* 2018, **20**, 30304-30311.

9. Y. Wu, H. Li and J. Hou, *Comp. Mater. Sci.* 2021, **190**, 110273.

10. M. Qiu, L. Ma, P. Sun, Z. Wang, G. Cui and W. Mai, *Nano-Micro Letters*. 2022, **14***, 31.

11. A. Bayaguud, X. Luo, Y. P. Fu and C. B. Zhu, *ACS Energy Lett.* 2020, **5**, 3012.

12. R. R. Zhao, Y. Yang, G. X. Liu, R. J. Zhu, J. B. Huang, Z. Y. Chen, Z. H. Gao, X. Chen and L. Qie, *Adv. Funct. Mater.* 2021, **31**, 2001867

13. R. Yao, L. Qian, Y. Sui, G. Zhao, R. Guo, S. Hu, P. Liu, H. Zhu, F. Wang, C. Zhi and C. Yang, *Adv. Energy. Mater.* 2021, **12**, 2102780.

14. P. Sun, L. Ma, W. Zhou, M. Qiu, Z. Wang, D. Chao and W. Mai, *Angew. Chem. Int. Ed.* 2021, **60**, 18247.

15. D. Yuan, J. Zhao, H. Ren, Y. Chen, R. Chaua, E. Tang, Y. Cai, E. Edison, W. Manalastas, M. Wong and M. Srinivasan, *Angew. Chem. Int. Ed.* 2021, **60**, 7213.

16. M. Qiu, H. Jia, C. Lan, H. Liu and S. Fu, *Energy Storage Mater.* 2022, **45**, 1175.

17. N. Chang, T. Li, R. Li, S. Wang, Y. Yin, H. Zhang and X. Li, *Energy Environ. Sci.*, 2021, **13**, 3527.

18. X. Guo, Z. Zhang, J. Li, N. Luo, G.-L. Chai, T. Miller, F. Lai, P. Shearing, D. Brett, D. Han, Z. Weng, G. He and L. Parkin, *ACS Energy Lett*. 2021, **6**, 395.

19. Y. Li, P. Wu, W. Zhong, C. Xie, Y. Xie, Q. Zhang, D. Sun, Y. Tang and H. Wang, *Energy Environ. Sci.*, 2021, **14**, 5563.

20. X. Zeng, J. Mao, J. Hao, J. Liu, S. Liu, Z. Wang, Y. Wang, S. Zhang, T. Zheng, J. Liu, P. Rao and Z. Guo, *Adv. Mater*. 2021, **33**, 2007416.

21. J. Shi, T. Sun, J. Bao, S. Zheng, H. Du, L. Li, X. Yuan, T. Ma and Z. Tao, *Adv. Funct. Mater*. 2021, **31**, 2102035.

22. W. Xu, K. Zhao, W. Huo, Y. Wang, G. Yao, X. Gu, H. Cheng, L. Mai, C. Hu and X. Wang, *Nano Energy*, 2019, **62**, 275.

23. W. Yang, X. Du, J. Zhao, Z. Chen, J. Li, J. Xie, Y. Zhang, Z. Cui, Q. Kong, Z. Zhao, C. Wang, Q. Zhang and G. Cui, *Joule*. 2020, **4**, 1557.

24. Y. Zeng, X. Zhang, R. Qin, X. Liu, P. Fang, D. Zheng, Y. Tong and X. Lu, *Adv. Mater*. 2019, **31**, 1903675.

25. A. Bayaguud, X. Luo, Y. Fu and C. Zhu, *ACS Energy Lett.* 2020, **5**, 3012.

26. Y. Hao, D. Feng, L. Hou, T. Li, Y. Jiao and P. Wu, *Adv. Sci.* 2022, **9**, 2104832.

27. S.-J. Zhang, J. Hao, D. Luo, P.-F. Zhang, B. Zhang, K. Davey, Z. Lin and S.-Z. Qiao, *Adv. Energy. Mater.* 2021, **11**, 2102010.

28. C. Li, A. Shyamsunder, A. Hoane, D. M. Long, C. Y. Kwok, P. G. Kotula, K. R. Zavadil, A. A. Gewirth and L. F. Nazar, *Joule*. 2022, **6**, 1103-1120.

29. D. Xie, Y. Sang, D.-H. Wang, W.-Y. Diao, F.-Y. Tao, C. Liu, J.-W. Wang, H.-Z. Sun, J.-P. Zhang and X.-L. Wu, *Angew. Chem. Int. Ed.* 2022, e202216934.

30. Z. Miao, F. Zhang, H. Zhao, M. Du, H. Li, H. Jiang, W. Li, Y. Sang, H. Liu and S. Wang, *Adv. Funct. Mater.* 2022, **32**, 2111635.

31. H. Liu, J.-G. Wang, W. Hua, L. Ren, H. Sun, Z. Hou, Y. Huan, Y. Cao, C. Wei and F. Kang, *Energy Environ. Sci.*, 2022, **15**, 1872.

32. J. Zhang, Y. Wu, H. Xie, Y. Zeng, W. Liu, A. Gandi, Z. Qi, Z. Wang and H. Liang, *ACS Nano* 2023, **17**, 337-345.